Batteries & Supercaps

Research Article
doi.org/10.1002/batt.202400413

Chemistry
Europe
European Chemical
Societies Publishing

MnO Modified Porous Carbon with Improved Adsorption Capability and Promoted Redox Kinetics in Lithium-Sulfur Batteries

Chen Liang,[a, c] Jiangyan Xue,*[b] Zhongkai Wang,[a, c] Jingjing Xu,*[a, b] and Xiaodong Wu*[a, b, c]

Lithium-sulfur (Li–S) batteries are recognized as one of the most promising next-generation battery systems. However, the severe shuttle effect poses a crucial challenge for its large scale application. Herein, through simple freeze-drying and subsequently annealing, the MnO was utilized to modify porous carbon and thereby form stable bond order toward lithium polysulfides (LiPSs), thus inhibiting the shuttle effect. Besides, the MnO nanoparticles can increase the reaction sites, accelerate the kinetic conversion of LiPSs, facilitate the formation and decomposition of Li_2S during discharging and charging. Benefit from the merits of MnO mentioned above together with the physical confinement derived from porous carbon, the Li–S battery assembled with S@MnO–C cathode delivers excellent performance both in rate capacity and long-cycling, with a high capacity of 555 $mAh\,g^{-1}$ after 200 cycles at 0.3 C. This work broadens the potential and enlightens the strategy for designing efficient cathodes toward Li–S sulfur batteries.

Introduction

Since its commercialization in 1990s, lithium-ion batteries (LIBs) have attracted worldwide attention as they greatly meet the needs of portable electronic devices and electric vehicles.[1] Unfortunately, the specific capacity of cathodes based on intercalation chemistry is far from the desirableness of extending the driving range with the prosperity of electric vehicle market.[2] To address this issue, scientists have devoted great efforts to explore next-generation battery systems. Lithium-sulfur (Li–S) batteries based on a cathodic multi-electron conversion reaction with high theoretical capacities of 1675 $mAh\,g^{-1}$ and large potential energy densities of 2600 $Wh\,kg^{-1}$ have been considered as potential alternative to LIBs.[3] While the actual appliactions of Li–S batteries are obstructed by several challenges, including insulating feature of the charge-discharge products (S and Li_2S/Li_2S_2), serious volume expansion during cycling (80 %), severe shuttle effect caused by soluble lithium polysulfides (LiPSs) and sluggish reaction kinetics.[4]

To overcome the challenges mentioned above, strenuous efforts have been invested to fabricate plentiful host materials which are able to supress volume changes, capture LiPSs, facilitate charge transfer within the cathode and expedite the Li–S reaction velocity.[5] Thereinto, carbon materials have been widely exploited as sulfur host and conductive framework due to high conductivity and large surface area.[6] Nazar's group has made major breakthrough in this respect. In 2009, they fabricated CMK-3 with ordered mesoporous channels which can physically confine the diffusion of LiPSs and achieve a high discharge capacity of 1005 $mAh\,g^{-1}$ with a stable cycling for 20 cycles.[7] This work set off a wave of research on different carbon materials such as carbon nanotubes, graphene and porous carbon.[8]

However, carbon materials always have a nonpolar surface, which leads to weak interaction between carbon and polar LiPSs and limited inhibition of the LiPSs diffusion into electrolyte.[9] Then, polar nanostructured inorganic compounds with strong chemical adsorption including transition-metal oxides, sulfides, and carbides are introduced into sulfur host to block the diffusion of LiPSs more efficiently.[10] Nevertheless, with the deep understanding of mechanism, scientists realized that physical or chemical adsorption can't adrress shuttle effect, solve the low capacity and Coulombic efficiency at root due to the sluggish kinetics of sulfur species. Compared to non-polar carbon materials and polar materials, electrocatalytic materials which can accelerate the charge transfer and reaction rate and lower the energy barrier have been proven in favor of these processes.[11] Besides, the uniform distribution of catalytic sites can regulate the deposition of Li_2S/Li_2S_2. In hence, catalytic materials are focused in Li–S battery fields lately.

Metal oxide is one of the most common catalytic materials for sulfur cathode, which has attracted wide attention due to characteristics such as low cost, diverse species, simple

[a] C. Liang, Z. Wang, J. Xu, X. Wu
School of Nano-Tech and Nano-Bionics Department, University of Science and Technology of China, Hefei 230026, China
E-mail: jjxu2011@sinano.ac.cn
xdwu2011@sinano.ac.cn

[b] J. Xue, J. Xu, X. Wu
Suzhou Institute of Nano-Tech and Nano-Bionics (SINANO), Chinese Academy of Sciences, Suzhou 215123, China
E-mail: jyxue2022@sinano.ac.cn

[c] C. Liang, Z. Wang, X. Wu
Tianmu Lake Institute of Advanced Energy Storage Technologies, Liyang 213300, China

preparation, and controllable morphology.[12] Among them, manganese oxides (MnO_x) like Mn_2O_3, MnO_2 and Mn_3O_4 have been widely studied in the field of energy storage and conversion.[13] Nazar et al. synthesized manganese dioxide nanosheets to serve as the prototype and react with initially formed LiPSs to form surface-bound intermediates, which entraped polysulfides in the cathode and convert them on reduction to insoluble lithium sulfide via disproportionation.[14] Studies have found that unsaturated metal sites with low-valence state in metal-containing catalysts usually have higher oxidation activity than high-valence unsaturated metal sites.[15] Thus compared to other manganese oxides, MnO with low-cost and easy synthesis has great potential to hinder the shuttle effect and enable an efficient conversion to deliver fast kinetics of polysulfide redox reactions, but it is rarely studied due to its low conductivity.

Herein, through freeze-drying and subsequently annealing, we regulate the MnO nanoparticles with uniform and pony-size distrubution on porous carbon to alleviate the effect of conductivity. The prepared composite cathode can effectively increase the active sites, strongly adsorb LiPSs and accelerate the kinetic conversion of LiPSs, facilitate the formation and decomposition of Li_2S during discharging and charging. Thus the S@MnO–C cathode delivers a high capacity of 555 mAh g^{-1} after 200 cycles at 0.3 C. This work not only proposes a simple strategy to control the precise growth of catalyst, but also provides new ideas for the creation of efficient Li–S battery materials.

Materials and Methods

Synthesis of MnO–C

Typically, 0.57 g manganese acetate tetrahydrate ($Mn(OAc)_2\cdot 4H_2O$) and 3.00 g porous carbon were dissolved in 20 mL pure water in a beaker under stirring for 12 hours and ultrasonic for half an hour. Then the mixture was frozen at $-80\,°C$ and treated by freeze-drying for 12 hours to remove water. Finally, the product was calcined at $600\,°C$ under Ar atmosphere for 1 h with the heating rate of $5\,°C\,min^{-1}$.

Synthesis of S@MnO–C

MnO–C nanoparticles and sulfur were ground at a mass ratio of 3:2. Then the mixture was sealed at a stainless-steel vessel under Ar atmosphere, and heated in an oven at $155\,°C$ for 12 h.

Synthesis of Typical Cathode

The cathodes were prepared via mixing the synthesized S@MnO–C, LA133, and conductive carbon with a mass ratio of 20:2:3 in deionized water to generate a homogeneous slurry. The mixed slurry was then coated on carbon coated aluminium foil and dried at $80\,°C$ for 12 h. The dried foil sheets were cut into circular disks ($d = 12$ mm). The mass loading of active material is ~1.4 mg cm^{-2}.

Material Characterization

HITACHI Regulus8100 scanning electron microscope (SEM) and energy dispersive X-ray spectrometer (EDS) were used to detect the morphology and element distribution. X-ray photoelectron spectroscopy (XPS) analysis was performed at room temperature under inert atmosphere using a ULVAC-PHIPHI5000 Versa Probe III analytical spectrometer. Transmission electron microscope (TEM) images were obtained using a FEI Tecnai F20 transmission electron microscope. X-ray diffraction (XRD) measurements were conducted using D8Advance (Bruker) with Cu Kα radiation. Raman spectroscopy was analysed using Renishaw InViareflex. N_2 adsorption/desorption isotherms were performed with the 3H-2000PS2 (BSD Instrument) at 77 K. The specific surface areas are calculated by the Brunauer-Emmett-Teller (BET) method on the basis of the multipoint analysis. Thermogravimetric analysis (TGA) was carried out from 30 to $800\,°C$ at a heating rate of $10\,°C\,min^{-1}$ under air atmosphere.

Adsorption Capability Test

Li_2S_6 solution was prepared via the reaction of S and Li_2S with a fixed molar ratio of 5:1 in the dioxolane (DOL)/dimethyl ether (DME) solution (volume ratio 1:1) and stirred at $40\,°C$ for 12 h in the argon-filled glove box. Then the host material powders were added into the Li_2S_6 solution (5 mg/ml) and kept in the glove box for 12 h.

Catalysis of LiPSs

The catalytic effect of MnO on LiPSs conversion was evaluated by symmetric cell measurement and Li_2S deposition test. In detail, two pieces of the same electrode comprised of MnO–C or C prepared by blade coating were used as cathode and anode. 0.2 M Li_2S_6 solution was added into each coin cell, and then cyclic voltammetry (CV) measurements were performed at a scan rate of 1 mV s^{-1}.

For the Li_2S deposition test, Li_2S_8 solution (0.2 M) was first prepared by mixing sublimed S and Li_2S with a molar ratio of 7:1 in tetraethylene glycol dimethyl ether solution, which was vigorous magnetic stirring at $60\,°C$ for 24 h in the argon-filled glove box. The MnO–C or C as cathode, while lithium foil was used as anode to assemble the coin-type cell. 40 μL of the above Li_2S_8 electrolyte was dropped onto the cathode, and 30 μL electrolyte without Li_2S_8 was dropped on the anode side. The cells were galvanostatically discharged to 2.06 V under a current of 0.1 mA and then kept potentiostatically at 2.05 V until the current dropped below 10^{-5} A for nucleation and growth of Li_2S.

Electrochemical Testing

The electrochemical performance was evaluated by assembling cathode into CR2032 coin cells with Li metal as anode, 1 M LiTFSI solution with 2 wt% $LiNO_3$ in DOL and DME (volume ratio of 1:1) as electrolyte, and Celgard2325 membrane as separator. The batteries were then tested by galvanostatic charge and discharge test system (LAND, China) at room temperature. CV measurements were performed at different scan rates under the range of 1.7–2.8 V. Electrochemical impedance spectroscopy (EIS) was measured with the frequency range from 10^{-2} Hz to 10^5 Hz. Both CV and EIS were performed on the CHI660e electrochemical workstation. Potentiostatic intermittent titration technique (PITT) was conducted on Neware battery test system (CT-4000, Shenzhen Neware Technology Co. Ltd.).

Batteries & Supercaps

Research Article
doi.org/10.1002/batt.202400413

Chemistry Europe
European Chemical
Societies Publishing

Results and Discussion

Synthesis and Characterization

Figure 1a and Figure S1 illustrate the synthesis process of MnO—C through a two-step reaction. First, porous carbon and $Mn(OAc)_2 \cdot 4H_2O$ were dispersed in water under ultrasonic dispersion for 12 h to generate uniformly dispersed precursor. Then the precursor was treated by freeze-drying to remove solvents. Subsequently, the powder precursor was annealed at 600 °C for 1 h with heating rate of 5 °C min^{-1} under Ar atmosphere in a tube furnace to get the final product MnO—C. SEM and TEM were used to evaluate the material's architecture. As shown in Figure 1b and c, the morphology of MnO—C inherits the original porous carbon with smooth surface. It can be seen from EDS Mapping image that C, Mn and O distribute uniformly (Figure 1d). TEM image indicates that MnO is composed of particles with an average size of 30 nm and a good dispersion of Mn and O atoms (Figure 1e–g). High-resolution transmission electron microscope (HRTEM) image in Figure 1h reveals distinct lattice fringe of MnO with spacing of 0.22 nm, corresponding to the (200) facet of MnO.[16] Accord-

ing to the feed ratio during synthesis and TGA data (Figure S2), the content of MnO in the MnO—C is about 5%.

As further illustrated by XRD (Figure 2a), the MnO—C displays peaks at 34.9°, 40.5°, 58.7°, 70.1°, 73.8° and 87.7° attributed to the (111), (200), (220), (311), (222) and (400) lattice planes of MnO (PDF#07-0230), which is consistent with TEM results.[17] Raman spectra in Figure 2b display the D and G bands located at 1340 and 1585 cm^{-1}, which corresponds to the structural defects in graphitic structure and sp^2- bonded pairs. The I_D/I_G ratio for porous C and MnO—C is 1.43 and 1.46, indicating a slightly enhancement of defect degree in porous carbon skeleton with the MnO incorporation. Besides, we carried out electron paramagnetic resonance (EPR) test to observe the oxygen vacancy defects in MnO. Figure S3 can directly reflect the presence of oxygen vacancies on the MnO surface, which can provide more catalytic active sites during electrochemical reactions.[18] Figure S4 shows the N_2 adsorption/desorption isotherms and the derived Brunauer–Emmett–Teller (BET) surface areas and the Barrett-Joyner-Halenda (BJH) pore size distributions. The porous carbon we used in this work demonstrates the characteristics of micropores and large surface area with 1707 m^2 g^{-1}. The incorporation of MnO hasn't
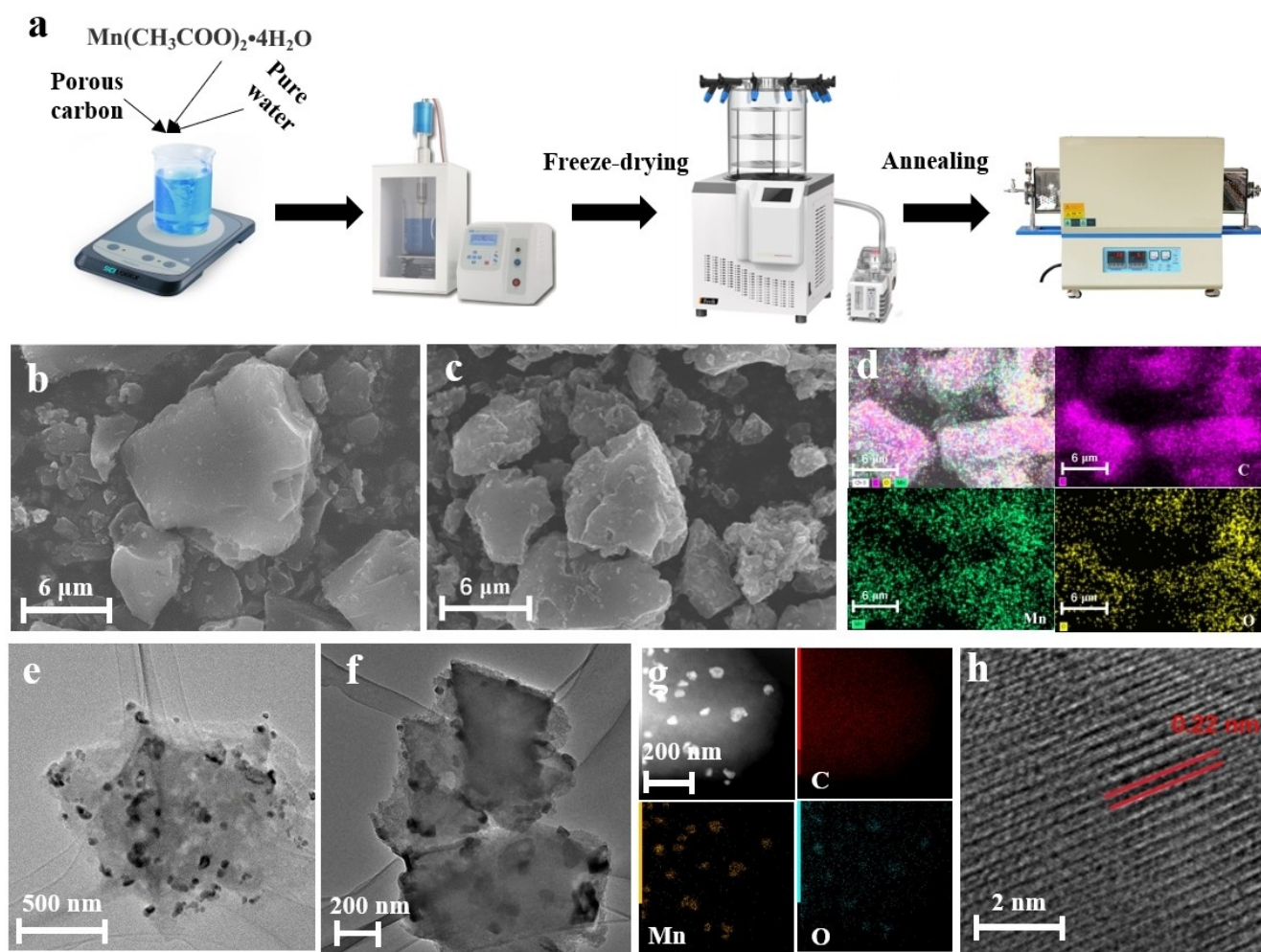

Figure 1. (a) Schematic illustration of the preparation of MnO—C. (b, c) SEM images of C and MnO—C. (d) EDS-Mapping image of MnO—C. (e, f) TEM images of MnO—C. (g) Scanning transmission electron microscopy (STEM) image and EDS elemental mapping images of MnO—C. (h) HRTEM image of MnO—C.
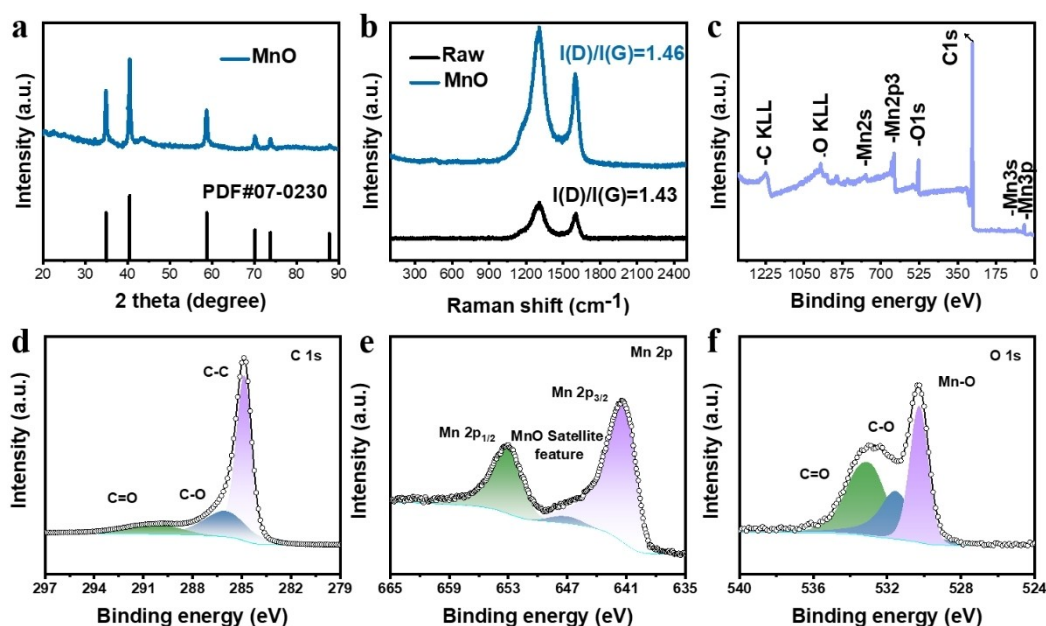
Figure 2. (a) XRD pattern of MnO–C. (b) Raman spectra. (c) XPS survey. High-resolution XPS spectrum of (d) C 1s, (e) Mn 2p and (f) O 1s.

destroyed the porous structure of C, thus MnO–C still possesses physical confinement to restrain the migration of LiPSs. To analyze the elemental composition and chemical states of material surface, XPS in Figure 2c–f was employed. The reference point for this analysis was the C 1s peak at 284.8 eV. The survey spectrum reveals the presence of C, Mn and O, indicating the successful incorporation of MnO into porous carbon framework. The peaks in high-resolution Mn 2p spectrum located at 641.5 eV and 653.2 eV can be ascribed to Mn^{2+} $2p_{3/2}$, Mn^{2+} $2p_{1/2}$.[19]

Catalytic Activity Characterization

First, we carried out EIS to observe the effect of MnO toward conductivity. As shown in Figure S5, the EIS changes slightly, indicating the introduction of MnO didn't apparently deteriorate the cell conductivity. Then, polysulfide adsorption, CV, nucleation and decomposition of Li_2S were carried out to evaluate the catalyst activity of MnO–C toward promoting the performance of Li–S batteries. To assess the ability of the MnO–C to trap polysulfides, an equal mass of porous C and MnO–C powder was introduced into an identical volume of a Li_2S_6 solution for 12 h. As shown in Figure 3a, the sample containing MnO–C became colorless while the color of original C was still yellow, demonstrating effective polysulfide adsorption of MnO. The influence of MnO in improving the Li–S reaction kinetics was further analyzed by CV. First, we used melt-diffusion approach to prepare the composite sulfur cathodes S/C and S/MnO–C with a sulfur loading of ≈ 1.4 $mg\,cm^{-2}$. Then we assembled these cathodes with Li metal anode and electrolyte (1 M LiTFSI in DME/DOL with 2 wt% $LiNO_3$) to obtain coin cells. All the CV curves display a pair of reduction peaks at 2.3 V (Cathodic I) and 2.0 V

(Cathodic II) which represent the conversion of S_8 to soluble long-chain Li_2S_x ($4 \leq x \leq 8$) and subsequent reduction to insoluble Li_2S_2/Li_2S, along with an anodic peak at 2.4 V indicating the oxidation of Li_2S to sulfur (Figure 3b and c). There is no obvious variation in oxidation peaks and current between the first and the next five cycles ascribed to the stable structure of MnO–C, suggesting that the electrode has a good reversibility of the reaction and cycling stability. Besides, the polarization of MnO–C is smaller than C, which proves that MnO–C is beneficial to the redox reaction process of Li–S battery. We further assembled symmetrical cells MnO–C | Li_2S_6 | MnO–C and C | Li_2S_6 | C to evaluate the redox reaction between LiPSs and cathodes. As shown in Figure 3d, the symmetrical cells exhibit 4 redox peaks, corresponding to the conversion between Li_2S_6–Li_2S, and Li_2S_6–S_8. Compared with the unmodified porous carbon, the MnO–C electrode exhibits higher redox current and accelerated redox kinetics. Besides, the MnO–C symmetrical cell shows the highest current and the sharpest redox peak, which can well balance the adsorption capacity and catalytic activity for LiPSs. Figure 3e–g depict a linear relationship between I_p and $v^{1/2}$ derived from the CV curves of various electrodes at different scan rates (Figure S6), thus the Li^+ diffusion coefficient can be approximately estimated by the slope value. The S@MnO–C electrode exhibits higher values for Cathodic I, Cathodic II and anodic II, indicating that MnO enables faster Li^+ diffusion and better kinetics for the redox reaction. Besides, to verify whether MnO contributes capacity in the battery, we assembled batteries with pure MnO–C cathode and tested its CV. As shown in Figure S7, the only reduction peak at 1.7 V belongs to the $LiNO_3$. In hence, MnO doesn't contribute capacity in the battery.

The effect of electrocatalyst on the nucleation and dissociation reactions of Li_2S was investigated by PITT. The
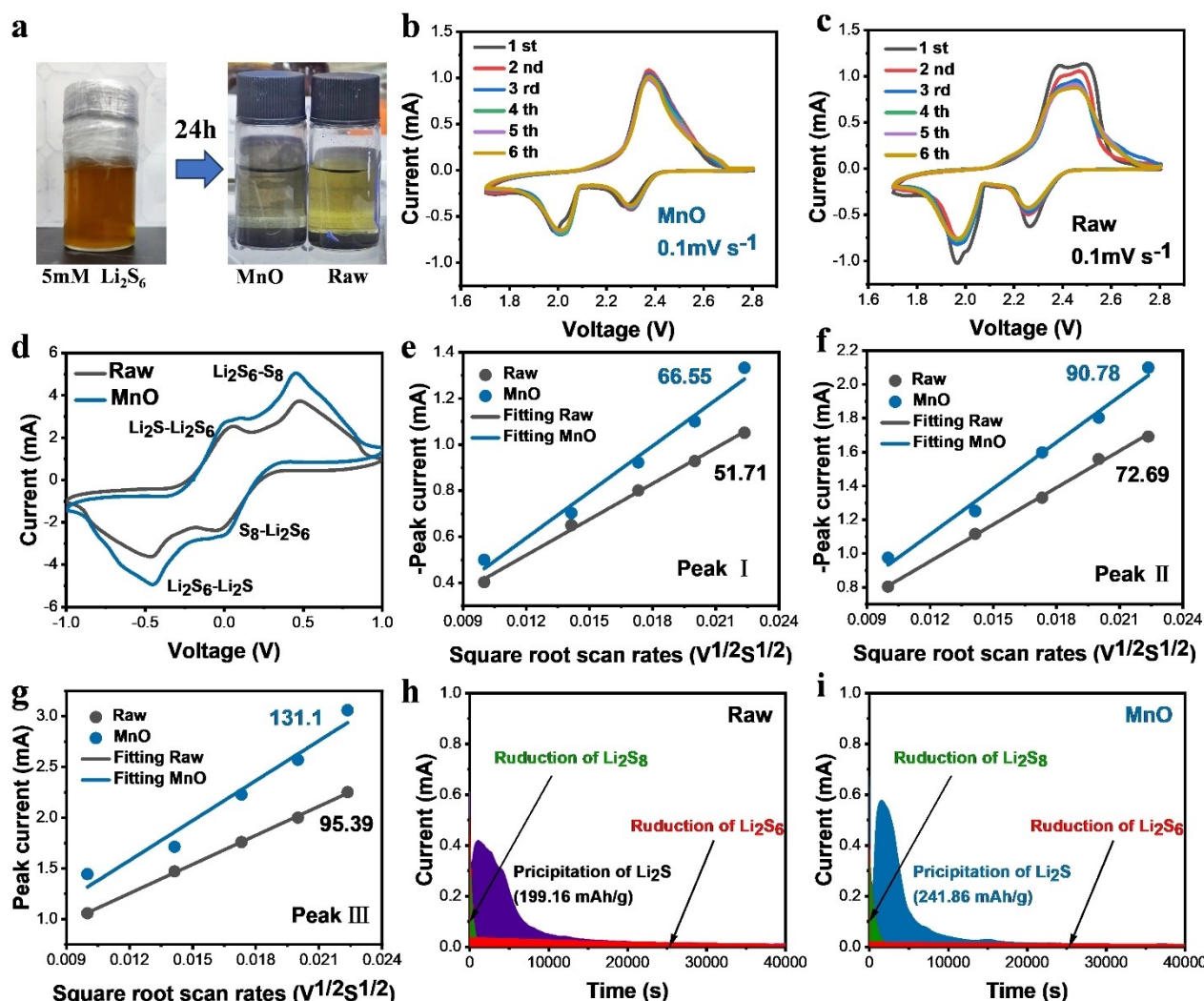
Figure 3. (a) Photographs of the Li_2S_6 solutions containing different adsorbing materials after overnight adsorption. (b, c) CV curves of MnO–C and C. (d) CV curves of Li_2S_6 symmetric cells. (e-g) Curves of the relationship between peak current and sweep speed. (h, i) Potentiostatic nucleation curves of Li_2S with C and MnO–C.

assembled battery was potentiostaticlly discharged in 50.0 mV intervals at voltage range from 2.25 to 1.8 V, and the current response to voltage pulses was shown in Figure S8. It can be seen clearly from Figure S9 that during the Li_2S nucleation process, the MnO–C electrode shows earlier nucleation, promoting the reaction process. Besides, Figure S10 compares the amplified discharge curve and MnO–C reveals the smaller nucleation overpotential of 10.7 mV than C (31.7 mV). In the following characterization, we carried out chronoamperometry tests to reveal Li_2S nucleation and dissolution efficiency, which ultimately governs the rate of discharge and charge reactions. As shown in Figure 3h and i, the monotonic decrease in the initial current ascribes to the conversion from Li_2S_8 to Li_2S_4 and subsequent current peak corresponds to the further nucleation and growth of insoluble Li_2S. MnO–C electrode exhibits higher precipitation peak ($I_p = 0.8$ mA) and faster nucleation time, indicating the rapid nucleation of insoluble Li_2S. Based on the Faraday's law, the precipitation capacity is attributed to the integral area under the curves. The specific capacity based

on the content of sulfur in the electrolyte of Li_2S precipitation on MnO–C (241.86 mA cm^{-2}) greatly exceeds that of porous C (199.16 mA cm^{-2}), confirming its more remarkable kinetics and catalytically active in converting LiPSs to Li_2S due to the incorporation of MnO.

Electrochemical Performance

To explore the practical use advantage of MnO–C as an efficient electrocatalyst within sulfur cathodes in Li–S batteries, S@MnO–C cathodes were assembled with celgard2325 separators and lithium foils anodes using CR2025 coin-type prototype cells which rate and cycle performance were tested. As a reference, cells based on S@C cathodes were also assembled and evaluated. The rate performances of Li-S batteries are estimated at current densities ranging from 0.05 to 1.50 C. As shown in Figure 4a, MnO–C cathode displays
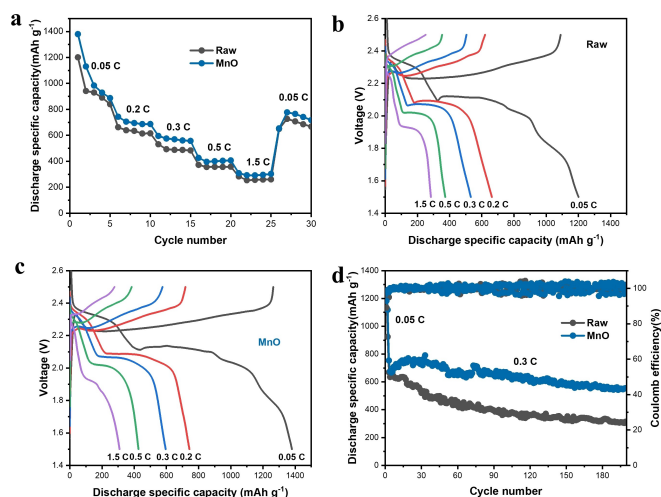
Batteries & Supercaps

Research Article
doi.org/10.1002/batt.202400413

Chemistry Europe
European Chemical
Societies Publishing

Figure 4. (a) Rate performance with various cathodes. (b, c) First galvanostatic curves of various cathodes at different rates. (d) Long-term cycling performance of the S@MnO–C electrode at 0.3 C.

specific capacities of 1400, 743, 595, 426, and 308 mAh g^{-1} at 0.05, 0.2, 0.3, 0.5 and 1.5 C, respectively.

The polarization voltage (ΔE) is here defined as the potential difference between the charge and discharge platforms at 50% charge/discharge capacity. The cathodes composed of MnO–C exhibits lower polarization overpotential than porous carbon, indicating enhanced kinetics in Li–S reaction (Figure 4b and c). In Figure 4d, the S@MnO–C delivers an outstanding long-term stability and it maintains 555 mAh g^{-1} after 200 cycles at 0.3 C, which are obviously better than the S@C||Li battery and many Li–S batteries reported before (Table S1). Such outstanding cycle performance confirms that MnO–C can enhance the catalytic conversion of LiPSs and inhibit the shuttle effect of LiPSs in the cycling procedure. The synthesis method we proposed in this work is simple and universal, indicates its great development potential in large-scale synthesis. Besides, the production cost of carbon substrate and catalyst we used are very low, which is beneficial to realize commercial application. In hence, we believe that the system we proposed in this work has great application prospect.

Conclusions

In conclusion, to improve the electrochemical performance of Li-S batteries, MnO modified porous carbon with uniform dispersion was fabricated through a facile freeze-drying and one-step annealing method in this work. Comparative electrochemical analyses showed that MnO exhibits abundant active sites with effectively capture ability toward soluble sulfur species, which is beneficial to the redox kinetics of the polysulfides conversion and can improve the utilization of the active material. As a result, the S@MnO–C cathode base battery achieves a high capacity of 555 mAh g^{-1} after 200 cycles at 0.3 C. This work provides a simple method for the

design of high-performance cathodes for Li–S batteries and has certain enlightenment significance for the future commercial prospects.

Conflict of Interests

The authors declare no conflict of interest.

Data Availability Statement

Research data are not shared.

[1]   J. B. Goodenough, K.-S. Park, *J. Am. Chem. Soc.* **2013**, *135*, 1167.
[2]   W. Zhong, C. Zhang, S. Li, W. Zhang, Z. Zeng, S. Cheng, J. Xie, *Sci. China Mater.* **2023**, *66*, 903–912.
[3]   a) C. X. Bi, M. Zhao, L. P. Hou, Z. X. Chen, X. Q. Zhang, B. Q. Li, H. Yuan, J. Q. Huang, *Adv. Sci.* **2022**, *9*, 2103910; b) L. Zhou, D. L. Danilov, F. Qiao, J. Wang, H. Li, R. A. Eichel, P. H. L. Notten, *Adv. Energy Mater.* **2022**, *12*, 2202094; c) M. A. Pope, I. A. Aksay, *Adv. Energy Mater.* **2015**, *5*, 1500124.
[4]   a) A. Manthiram, Y. Fu, Y. Su, *Acc. Chem. Res.* **2013**, *46*, 1125; b) T. Lei, W. Chen, W. Lv, J. Huang, J. Zhu, J. Chu, *Joule* **2019**, *3*, 2091–2104; c) B. He, W. C. Li, C. Yang, S. Q. Wang, A. Lu, *ACS Nano* **2016**, *26*, 1633–1639; d) W. Li, H. Yao, K. Yan, G. Zheng, Z. Liang, Y. M. Chiang, *Nat. Commun.* **2015**, *6*, 7436.
[5]   C. Zhao, F. Huo, Y. Yang, J. Ruan, F. Chai, H. Xu, Y. Liu, L. Zhang, A. Cabot, Z. Sun, Y. Zhang, *Adv. Funct. Mater.* **2024**, 2402175.
[6]   C. Lu, Y. Chen, Y. Yang, X. Chen, *Nano Lett.* **2020**, *20*, 5522.
[7]   X. L. Ji, K. T. Lee, L. F. Nazar, *Nat. Mater.* **2009**, *8*, 500–506.
[8]   a) H. Peng, J. Huang, M. Zhao, Q. Zhang, X. Cheng, X. Liu, W. Qian, F. Wei, *Adv. Funct. Mater.* **2024**, *24*, 2772–2781; b) G. Zhou, E. Paek, G. S. Hwang, A. Manthiram, *Adv. Energy Mater.* **2016**, *6*, 1501355; c) X. Li, Y. Cao, W. Qi, L. V. Saraf, J. Xiao, Z. Nie, J. Mietek, J. Zhang, B. Schwenzer, J. Liu, *J. Mater. Chem.* **2011**, *21*, 16603.
[9]   Z. Yang, R. Xiao, X. Zhang, X. Wang, D. Zhang, Z. Sun, F. Li, *Energy Environ. Mater.* **2022**, *5*, 693–710.
[10]   a) X. Liu, J.-Q. Huang, Q. Zhang, L. Mai, *Adv. Mater.* **2017**, *29*, 1601759; b) P. Li, L. Ma, T. Wu, H. Ye, J. Zhou, F. Zhao, N. Han, Y. Wang, Y. Wu, Y. Li, J. Lu, *Adv. Energy Mater.* **2018**, *8*, 1800624; c) D. Ma, Y. Li, J. Yang, H. Mi, S. Luo, L. Deng, C. Yan, M. Rauf, P. Zhang, X. Sun, X. Ren, J. Li, H. Zhang, *Adv. Funct. Mater.* **2018**, *28*, 1705537.
[11]   a) M. Tahir, L. Pan, F. Idrees, X. Zhang, L. Wang, J.-J. Zou, Z. L. Wang, *Nano Energy* **2017**, *37*, 136; b) L. Zhang, J. Xiao, H. Wang, M. Shao, *ACS Catal.* **2017**, *7*, 7855.
[12]   X. Liu, J. Q. Huang, Q. Zhang, L. Mai, *Adv. Mater.* **2017**, *29*, 1601759.
[13]   a) J. Guo, X. Zhang, X. Du, F. Zhang, *J. Mater. Chem.* **2017**, *5*, 6447–6454; b) A. S. Ryabova, S. Y. Istomin, K. A. Dosaev, A. Bonnefont, J. Hadermann, N. A. Arkharova, A. S. Orekhov, R. P. Sena, V. A. Saveleva, G. Kerangueven, E. V. Antipov, E. R. Savinova, G. A. Tsirlina, *Electrochim. Acta* **2021**,

Batteries & Supercaps

Research Article
doi.org/10.1002/batt.202400413

Chemistry
Europe
European Chemical
Societies Publishing

367, 137378; c) M. Y. Wu, Y. H. Kwok, Y. G. Zhang, W. Szeto, H. B. Huang, D. Y. C. Leung, *Chem. Eng. Sci.* **2021**, *231*, 116288.

[14] X. Liang, C. Hart, Q. Pang, A. Garsuch, T. Weiss, L. F. Nazar, *Nat. Commun.* **2015**, *6*, 5682.

[15] H. Jalife-Jacobo, R. Feria-Reyes, O. Serrano-Torres, S. Gutierrez-Granados, J. M. Peralta-Hernandez, *J. Hazard Mater.* **2016**, *319*, 78–83.

[16] X. Gong, R. Li, H. Chen, C. He, Z. A. Gao, H. Xie, *Arab. J. Chem.* **2023**, *16*, 104752.

[17] Y. Feng, H. Liu, Q. Lu, Y. Liu, J. Li, X. He, X. Liu, D. Mikhailova, *J. Power Sources* **2022**, *520*, 230885.

[18] F. Zheng, Z. Yin, H. Xia, G. Bai, Y. Zhang, *Chem. Eng. J.* **2017**, *327*, 474–480.

[19] S. Ru, H. Xiao, G. Ma, J. Tan, X. Wang, Z. Ai, *Mater. Lett.* **2020**, *276*, 128244.